THE JOURNAL OF PHYSICAL CHEMISTRY C

Article

Cite This: J. Phys. Chem. C 2018, 122, 15198−15207

pubs.acs.org/JPCC

Nature of Decahydro-*closo*-decaborate Anion Reorientations in an Ordered Alkali-Metal Salt: $Rb_2B_{10}H_{10}$

Mirjana Dimitrievska,*[,†,‡] Vitalie Stavila,[§] Alexei V. Soloninin,[∥] Roman V. Skoryunov,[∥] Olga A. Babanova,[∥] Hui Wu,[†] Wei Zhou,[†] Wan Si Tang,[†,⊥,#] Antonio Faraone,[†] Jacob D. Tarver,[†,‡] Benjamin A. Trump,[†] Alexander V. Skripov,*[,∥] and Terrence J. Udovic*[,†]

[†]NIST Center for Neutron Research, National Institute of Standards and Technology, Gaithersburg, Maryland 20899-6102, United States

[‡]National Renewable Energy Laboratory, Golden, Colorado 80401, United States

[§]Energy Nanomaterials, Sandia National Laboratories, Livermore, California 94551, United States

[∥]Institute of Metal Physics, Ural Division of the Russian Academy of Sciences, Ekaterinburg 620108, Russia

[⊥]Department of Materials Science and Engineering, University of Maryland, College Park, Maryland 20742-2115, United States

[#]Geophysical Laboratory, Carnegie Institution of Washington, Washington DC 20015, United States

Supporting Information

ABSTRACT: The ordered monoclinic phase of the alkali-metal decahydro-*closo*-decaborate salt $Rb_2B_{10}H_{10}$ was found to be stable from about 250 K all the way up to an order−disorder phase transition temperature of ≈762 K. The broad temperature range for this phase allowed for a detailed quasielastic neutron scattering (QENS) and nuclear magnetic resonance (NMR) study of the protypical $B_{10}H_{10}^{2-}$ anion reorientational dynamics. The QENS and NMR combined results are consistent with an anion reorientational mechanism comprised of two types of rotational jumps expected from the anion geometry and lattice structure, namely, more rapid 90° jumps around the anion C_4 symmetry axis (e.g., with correlation frequencies of $\approx 2.6 \times 10^{10}$ s^{-1} at 530 K) combined with order of magnitude slower orthogonal 180° reorientational flips (e.g., $\approx 3.1 \times 10^{9}$ s^{-1} at 530 K) resulting in an exchange of the apical H (and apical B) positions. Each latter flip requires a concomitant 45° twist around the C_4 symmetry axis to preserve the ordered $Rb_2B_{10}H_{10}$ monoclinic structural symmetry. This result is consistent with previous NMR data for ordered monoclinic $Na_2B_{10}H_{10}$, which also pointed to two types of anion reorientational motions. The QENS-derived reorientational activation energies are 197(2) and 288(3) meV for the C_4 fourfold jumps and apical exchanges, respectively, between 400 and 680 K. Below this temperature range, NMR (and QENS) both indicate a shift to significantly larger reorientational barriers, for example, 485(8) meV for the apical exchanges. Finally, subambient diffraction measurements identify a subtle change in the $Rb_2B_{10}H_{10}$ structure from monoclinic to triclinic symmetry as the temperature is decreased from around 250 to 210 K.

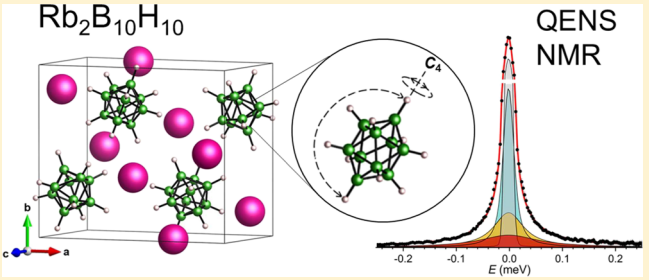

INTRODUCTION

Anions and cations typically bind together via coulombic forces to form translationally rigid crystalline solids. Moreover, if either or both happen to be polyatomic ions (e.g., SiH_3^-, BH_4^-, $B_{10}H_{10}^{2-}$, $B_{12}H_{12}^{2-}$, or NH_4^+), then the otherwise rather translationally immobile ions are nonetheless still capable of significant orientational mobility.[1−7] This mobility can have profound effects on compound properties. For example, in the novel solid superionic conducting salts, $Na_2B_{12}H_{12}$ (ref 8) and $Na_2B_{10}H_{10}$,[9] there are indications that the orientational mobilities of the polyhedral $B_{12}H_{12}^{2-}$ and $B_{10}H_{10}^{2-}$ anions can facilitate cation conductivity via an anion-rotation−cation-translation cooperative effect,[10−12] especially after transitions to higher-entropy, disordered phases.[8,9]

In $Na_2B_{10}H_{10}$, this transition occurs between around 360 and 380 K,[9,13] at which point, the ordered monoclinic structure[14] with a fully occupied cation sublattice changes to a disordered face-centered cubic arrangement of roughly two orders of magnitude more orientationally mobile decahydro-*closo*-decaborate ($B_{10}H_{10}^{2-}$) anions ($\gg 2-3 \times 10^{10}$ jumps s^{-1}) and a cation vacancy-rich sublattice enabling liquid-like Na^+ translational jump diffusion ($>2 \times 10^8$ jumps s^{-1}) exhibiting exceptional superionic conductivity (e.g., 0.01 S cm^{-1} at 383 K).[4,9] The two key complementary techniques used to characterize the details of these $B_{10}H_{10}^{2-}$ orientational

Received: May 8, 2018
Revised: June 8, 2018
Published: June 11, 2018

DOI: 10.1021/acs.jpcc.8b04385
J. Phys. Chem. C 2018, 122, 15198−15207

mobilities in $Na_2B_{10}H_{10}$ were incoherent quasielastic neutron scattering (QENS) and nuclear magnetic resonance (NMR). NMR can probe various atomic jump rates over the dynamic range of $\sim 10^4$ to 10^{11} s^{-1}, whereas QENS is particularly sensitive to H jump rates over the dynamic range of $\sim 10^8$ to 10^{12} s^{-1}. Although NMR possesses a broader dynamical reach than QENS, the latter has the advantage of being able to provide direct insights concerning the mechanistic nature of the investigated motions.

Despite being able to probe the complex nature of the $B_{10}H_{10}^{2-}$ anion motions in the disordered superionic phase of $Na_2B_{10}H_{10}$,[4] the relatively low order−disorder phase transition temperature for this compound (and thus the relatively low anion mobility, $<10^8$ reorientational jumps s^{-1}, outside of the QENS measurement window) precluded any practical QENS investigation of the anion reorientational mechanism in the ordered monoclinic phase. NMR results for this phase hinted at the presence of two distinct types of reorientational motions consistent with the ordered nature of the structure and the D_{4d} anion symmetry.[4] In the present paper, we address this shortcoming by diverting our investigation to a heavier alkali-metal congener of $Na_2B_{10}H_{10}$, namely, $Rb_2B_{10}H_{10}$, which we show maintains its ordered monoclinic structure from around 250 K to temperatures approaching 762 K. With this extended temperature range of stability for its ordered phase, much higher anion mobilities could be thermally induced, enabling us to investigate more fully with both QENS and NMR, the mechanistic and energetic details of $B_{10}H_{10}^{2-}$ anion reorientational motions within an ordered (monoclinic) alkali-metal decahydro-*closo*-decaborate structure, rather than within a disordered phase. Our results corroborate the existence of the two possible types of symmetry-allowed reorientational jumps: (i) 90° rotations around the anion C_4 symmetry axis and (ii) 180° orthogonal flips of this C_4 axis combined with an additional 45° C_4 rotation.

EXPERIMENTAL METHODS

^{11}B-enriched $Rb_2{}^{11}B_{10}H_{10}$, free of the neutron-absorbing ^{10}B isotope comprising 20% of natural boron, was used for neutron scattering measurements. $Rb_2B_{10}H_{10}$ with natural boron was used for NMR and differential scanning calorimetry (DSC) measurements. $Rb_2{}^{11}B_{10}H_{10}$ was synthesized by first forming $(Et_3NH)_2{}^{11}B_{10}H_{10}$ from $^{11}B_{10}H_{14}$ (Katchem[15]) and triethylamine, converting it to $(H_3O)_2{}^{11}B_{10}H_{10}$ and neutralizing the acidic solution with 0.1 M RbOH to a pH of 7, and drying the resulting aqueous $Rb_2{}^{11}B_{10}H_{10}$ first with a rotary evaporator at 323 K to form a solid hydrate followed by complete dehydration under vacuum at 473 K for 16 h. $Rb_2B_{10}H_{10}$ (with natural boron) was made in a similar fashion using $B_{10}H_{14}$ (Sigma-Aldrich). X-ray powder diffraction (XRPD) measurements for each synthesized compound (using a Rigaku Ultima III X-ray diffractometer with a Cu Kα source) yielded the expected room-temperature monoclinic powder pattern.[16] Further variable-temperature synchrotron XRPD (SXRPD) measurements of $Rb_2{}^{11}B_{10}H_{10}$, loaded into a quartz capillary, were performed between 100 and 450 K at the Advanced Photon Source on beamline 17-BM-B at Argonne National Laboratory [λ = 0.45220(1) Å]. Data were collected using a two-dimensional amorphous Si-plate detector with the two-dimensional data converted to one-dimensional data using GSAS-II.[17] Rietveld structural refinements were performed using the GSAS package.[18]

All neutron scattering measurements were performed at the National Institute of Standards and Technology Center for Neutron Research using 0.65 g of $Rb_2{}^{11}B_{10}H_{10}$ mounted in a thin-walled annular geometry (5 cm height × 1.2 cm annulus diameter) inside a helium-filled, o-ring-sealed, cylindrical Al sample cell. Depending on the maximum measurement temperature, the o-ring material was either In (below 400 K) or Pb (below 580 K). Above 580 K, no seal was used and the sample was measured in a vacuum. Neutron powder diffraction (NPD) measurements were performed between 7 and 300 K on the BT-1 High-Resolution Neutron Powder Diffractometer[19] with the Cu(311) monochromator at λ = 1.5397(2) Å and an in-pile collimation of 60 min of arc. Neutron vibrational spectroscopy (NVS) measurements were performed at 4 K on the Filter-Analyzer Neutron Spectrometer[20] using the Cu(220) monochromator with pre- and post-collimations of 20′ of arc, yielding a full width at half-maximum (fwhm) energy resolution of about 3% of the neutron energy transfer. QENS measurements were performed up to 680 K on three complementary instruments: the Disc Chopper Spectrometer (DCS)[21] between 100 and 680 K using incident neutron wavelengths (λ) of 4.08 Å (4.91 meV) and 10 Å (0.82 meV) with respective resolutions of 89 and 17 μeV fwhm and respective maximum attainable Q values of around 2.89 and 1.18 $Å^{-1}$; the High Flux Backscattering Spectrometer (HFBS)[22] between 80 and 530 K [plus up to 580 K during an elastic-scattering fixed-window scan (FWS)] using an incident neutron wavelength of 6.27 Å (2.08 meV) with a resolution of 0.8 μeV fwhm and a maximum attainable Q value of 1.75 $Å^{-1}$; and the NGA Neutron Spin-echo Spectrometer (NSE)[23] at 4, 365, and 380 K using an incident neutron wavelength of 5.0 Å (3.27 meV, $\Delta\lambda/\lambda \approx 0.17$) for Fourier times up to 10 ns at a Q value of 1.55 $Å^{-1}$, where coherent scattering contributions were negligible. Instrumental resolution functions were determined from QENS spectra at lower temperatures free of quasielastic scattering, i.e., below 200 K for DCS data, 245 K for HFBS data, and 4 K for NSE data. QENS data were analyzed using the DAVE software package.[24] ^{1}H NMR measurements were performed on the pulse spectrometer described elsewhere[25] at resonance frequencies of 14, 28, and 90 MHz. Nuclear spin−lattice relaxation rates were measured using the saturation−recovery method. NMR spectra were recorded by Fourier transforming the solid echo signals. DSC measurements with simultaneous thermogravimetric analysis (TGA) were made with a Netzsch (STA 449 F1 Jupiter) TGA−DSC under He flow with Al sample pans.

To aid the structural model refinements of the diffraction data, first-principles calculations were performed within the plane-wave implementation of the generalized gradient approximation to density functional theory (DFT) using a Vanderbilt-type ultrasoft potential with Perdew−Burke−Ernzerhof exchange.[26] A cutoff energy of 544 eV and a 2 × 2 × 4 k-point mesh (generated using the Monkhorst−Pack scheme) were used and found to be enough for the total energy to converge within 0.01 meV per atom. For comparison with the NVS measurements, simulated phonon densities of states (PDOSs) were generated from the DFT-optimized $Rb_2{}^{11}B_{10}H_{10}$ structure using the supercell method (1 × 1 × 2 cell size) with finite displacements[27,28] and were appropriately weighted to take into account the H, ^{11}B, and Rb total neutron scattering cross sections. In addition, simulated PDOSs of the "isolated" $^{11}B_{10}H_{10}^{2-}$ anions were generated for comparison

DOI: 10.1021/acs.jpcc.8b04385
J. Phys. Chem. C 2018, 122, 15198−15207

using 20 × 20 × 20 Å^3 supercells and considering their D_{4d} molecular symmetries in the phonon calculations.

Structural depictions were made using the Visualization for Electronic and Structural Analysis (VESTA) software.[29] For all figures, standard uncertainties are commensurate with the observed scatter in the data, if not explicitly designated by vertical error bars.

RESULTS AND DISCUSSION

$Rb_2B_{10}H_{10}$ Structural Behavior. A TGA−DSC scan for $Rb_2B_{10}H_{10}$ upon heating (10 K min^{-1}) up to 870 K (shown in Figure S1 of the Supporting Information) indicates an endothermic feature with an onset temperature of around 762 K marking a transition from the known room-temperature ordered monoclinic phase[16] (shown in Figure 1) to an

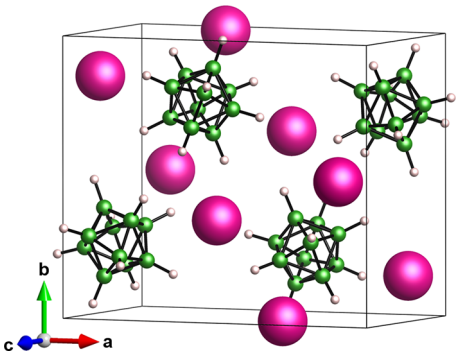

Figure 1. 298 K monoclinic ($P2_1/n$) $Rb_2B_{10}H_{10}$ structure from model refinement of the $Rb_2{}^{11}B_{10}H_{10}$ SXRPD data based on DFT optimization of the structure reported in ref 16. Magenta, green, and white spheres denote Rb, B, and H atoms, respectively.

unknown (likely disordered) phase, possibly analogous to that observed for $Rb_2B_{12}H_{12}$ near 742 K.[30] By 790 K, the compound starts to decompose with a loss of mass. Cycling below the decomposition temperature indicates that the transition is reversible and slightly hysteretic (also shown in Figure S1). The stability of the monoclinic phase at subambient temperatures was further investigated by SXRPD measurements down to 100 K. Indeed, the partial diffraction patterns versus temperature in Figure 2 signal the reversible transformation to a different structure upon cooling past around 250 K. The transformation appears to be of second order and is completed by around 210 K. No obvious transition is observed by TGA−DSC over this broad transformation range, suggesting that the magnitude of any enthalpic change is extremely small. Rietveld analyses of the SXRPD patterns above (at 450 and 298 K) and below (at 100 K) this subambient transition indicate that the change from the known monoclinic $P2_1/n$-symmetric structure[16] is rather subtle, involving a further lowering of the symmetry to $P\bar{1}$ via a slight triclinic distortion, i.e., from respective α, β, and γ values of 90°, 94.130(2)°, and 90° at 298 K to 90.348(9)°, 94.801(8)°, and 90.40(1)° at 100 K. Figure S2 depicts the model refinements of the SXRPD data at 450, 298, and 100 K. Table S1 and Supporting Information CIF files summarize the structural analysis details. Additional NPD measurements shown in Figure S3 of the strongest diffraction peaks versus temperature using DCS and the BT-1 diffractometer corroborate that the monoclinic phase remains stable up to

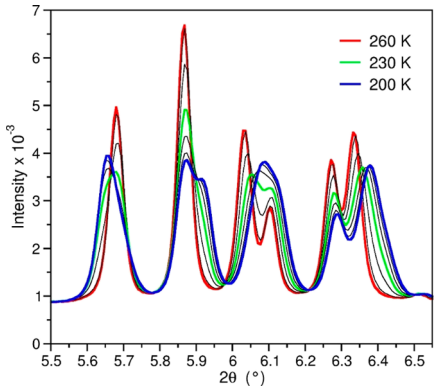

Figure 2. Progression of partial SXRPD patterns [λ = 0.45220(1) Å] with temperature in 10 K steps upon cooling from 260 to 200 K, showing the structural transformation from $P2_1/n$ symmetry to $P\bar{1}$ symmetry. Patterns at 260 K (red), 230 K (green), and 200 K (blue) are highlighted for clarity to distinguish from the intervening four patterns in black measured at 250, 240, 220, and 210 K.

at least 680 K and down to around 250 K and the lower-temperature triclinic phase remains stable down to at least 7 K.

The 4 K neutron vibrational spectrum for $Rb_2{}^{11}B_{10}H_{10}$ is shown in Figure S4 compared with one + two-phonon DFT-simulated spectra after energy optimizations of both the triclinic and monoclinic structures as well as the isolated $^{11}B_{10}H_{10}{}^{2-}$ anion, indicating reasonable agreement between experiment and theory and highlighting only very small differences expected in the PDOSs between the structurally similar triclinic and monoclinic phases. The DFT calculations suggest negligible energy differences between the 0 K energy-optimized triclinic and monoclinic structures within a computational accuracy of around ±20−30 meV/$Rb_2B_{10}H_{10}$ formula unit, which is in line with the absence of any obvious enthalpic feature accompanying this transition during the TGA−DSC measurements.

Proton NMR Measurements. The proton spin−lattice relaxation rates R_1^H measured at the resonance frequencies $\omega/2\pi$ = 14, 28, and 90 MHz for $Rb_2B_{10}H_{10}$ as functions of the inverse temperature are shown in Figure 3. Comparison of these results with the $R_1^H(T)$ data for a number of *closo*-poly(carba)borates[4,25,31] suggests that the observed proton

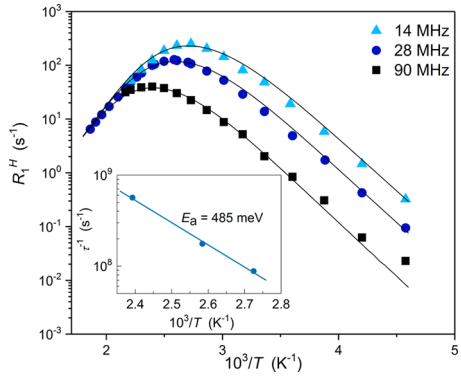

Figure 3. Proton spin−lattice relaxation rates measured at 14, 28, and 90 MHz for $Rb_2B_{10}H_{10}$ as functions of the inverse temperature. The black solid lines show the simultaneous fit of the model with a Gaussian distribution of activation energies to the data in the range of 219−537 K. The inset shows the Arrhenius plot of the H jump rates derived from the $R_1^H(T)$ maxima at different resonance frequencies.

DOI: 10.1021/acs.jpcc.8b04385
J. Phys. Chem. C 2018, 122, 15198−15207

spin−lattice relaxation rate in $Rb_2B_{10}H_{10}$ is governed by the nuclear dipole−dipole interaction modulated by reorientational motion of the complex anions. The temperature dependence of R_1^H is expected to pass through a maximum at the temperature at which the jump rate $\tau^{-1}(T)$ of anion reorientations becomes nearly equal to ω. Thus, the position of the $R_1^H(T)$ peak may be used to compare the jump rates in different materials: for compounds with faster motion, the $R_1^H(T)$ peak should be observed at lower temperatures. In particular, at $\omega/2\pi$ = 14 MHz, the $R_1^H(T)$ maximum in $Rb_2B_{10}H_{10}$ is observed at 367 K, whereas the corresponding maximum in $Rb_2B_{12}H_{12}$ occurs near 417 K.[25] Therefore, this indicates that the jump rates for the anion reorientations detected in $Rb_2B_{10}H_{10}$ are higher than those detected in its $B_{12}H_{12}$-based analogue. Yet we caution that the different compound structures and anion symmetries for $Rb_2B_{10}H_{10}$ and $Rb_2B_{12}H_{12}$ preclude any conclusion from the $R_1^H(T)$ data alone, concerning the types of reorientations sensed in each case.

According to the standard theory of nuclear spin−lattice relaxation due to atomic motion,[32] in the limit of slow motion ($\omega\tau \gg 1$), the relaxation rate R_1^H should be proportional to $\omega^{-2}\tau^{-1}$ and in the limit of fast motion ($\omega\tau \ll 1$), R_1^H should be proportional to τ, being frequency-independent. If the temperature dependence of the jump rate is governed by the Arrhenius law, $\tau^{-1} = \tau_0^{-1} \exp(-E_a/k_BT)$, with the activation energy E_a and the Boltzmann constant k_B, a plot of ln R_1^H versus T^{-1} is expected to be linear in the limits of both slow and fast motion with the slopes of $-E_a/k_B$ and E_a/k_B, respectively. Although the general features of the data presented in Figure 3 are correctly described by the standard theory,[32] the observed frequency dependence of R_1^H at T < 300 K appears to be somewhat weaker than the predicted ω^{-2} dependence for the slow-motion limit. This may indicate the presence of a certain distribution of the H jump rates.[33] The simplest approach to taking the distribution effects into account is based on the standard model with a Gaussian distribution of activation energies.[34] The corresponding motional parameters include an average activation energy $\overline{E}_a$, a distribution width (dispersion) ΔE_a, and a single value of the pre-exponential factor τ_0. For $Rb_2B_{10}H_{10}$, these model parameters have been varied to find the best fit to the experimental $R_1^H(T)$ data at three resonance frequencies simultaneously. The results of this simultaneous fit to the data in the range 219−537 K are shown by black curves in Figure 3. We have not observed any strong changes in the behavior of the proton spin−lattice relaxation rates below 250 K. This means that the subtle monoclinic-to-triclinic transition occurring between 250 and 210 K does not lead to any visible effects on the parameters of reorientational motion. The corresponding motional parameters are $\overline{E}_a$ = 522(7) meV, ΔE_a = 49(5) meV, and $\tau_0 = 7.6(6) \times 10^{-16}$ s. It should be noted that although the appearance of a certain jump rate distribution can be an indication of anions in slightly different environments due to such things as defects or impurities, it is more likely reflecting the presence of an additional jump process not resolved in the spin−lattice relaxation measurements. Indeed, if the difference between two frequency scales of H jump motion is relatively small (about one order of magnitude), an additional jump process may contribute only to the low-temperature slope of the single-peak $R_1^H(T)$ dependence, not leading to any additional peak. Similar behavior of $R_1^H(T)$ was reported for a number of Laves-phase hydrides showing two frequency scales of H jump motion.[35] Although for $Rb_2B_{10}H_{10}$, we cannot exclude other sources of a jump rate distribution; the presence of an additional jump process should be the main factor determining the observed deviations from the standard behavior of the proton spin−lattice relaxation rate (see QENS results below).

Apart from fitting the temperature dependences of R_1^H, the H jump rates τ^{-1} can also be determined from the positions of the $R_1^H(T)$ maxima at different resonance frequencies. This can be considered as a "model-independent" approach to estimates of the jump rates. Note that a presence of a Gaussian distribution of activation energies does not change the conditions of the $R_1^H(T)$ maxima.[33] In this case, the values of τ^{-1} should be considered as the most probable ones. The inset in Figure 3 shows the Arrhenius plot of the H jump rates derived from the positions of the $R_1^H(T)$ maxima at the three resonance frequencies. The activation energy obtained from this plot is 485(8) meV, which is rather close to the value of $\overline{E}_a$ derived above from the model fits.

Figure 4 shows the temperature dependence of the ^{1}H NMR line width Δ_H (fwhm). The observed behavior of $\Delta_H(T)$ for

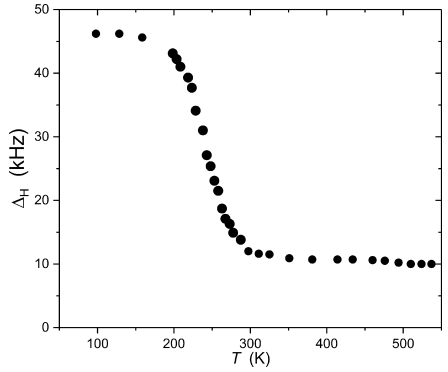

Figure 4. Temperature dependence of the width (fwhm) of the ^{1}H NMR line measured at 28 MHz for $Rb_2B_{10}H_{10}$.

$Rb_2B_{10}H_{10}$ is typical of compounds exhibiting thermally activated reorientational motion.[36] At low temperatures (T < 200 K), the line width is determined by the static dipole−dipole interactions between nuclear spins. The "rigid-lattice" second moment of the ^{1}H NMR line calculated on the basis of the $Rb_2B_{10}H_{10}$ triclinic structure is 2.03×10^{10} s^{-2}. Assuming that the line shape is Gaussian, this value of the second moment corresponds to Δ_H = 53.6 kHz, which is close to the experimental value of the line width (~46 kHz). It should be noted that the calculated "rigid-lattice" second moment is dominated by the "intramolecular" ^{1}H−^{11}B contribution (due to ^{1}H−^{11}B interactions within the same $B_{10}H_{10}$ group); this contribution gives about 81% of the total second moment. A significant drop of Δ_H related to motional narrowing[32] is observed near 235 K in Figure 4. Such a behavior indicates that near this temperature, the reorientational jump rate τ^{-1} in $Rb_2B_{10}H_{10}$ becomes close to the "rigid-lattice" value of the line width (in circular frequency units). A rough estimate of τ^{-1} based on the line-narrowing data gives ~10^5 s^{-1} at 235 K. The shape of the observed $\Delta_H(T)$ "step" is close to that expected for the thermally activated motional narrowing; we have not found any abrupt Δ_H changes due to the monoclinic-to-triclinic transition. For comparison, for $Rb_2B_{12}H_{12}$, a similar $\Delta_H(T)$ "step" is observed at higher temperatures (about 270 K).[25] This corresponds to the slower reorientational motion in $Rb_2B_{12}H_{12}$, in agreement with the spin−lattice relaxation data (see above). At T > 350 K, the line width nearly stops to

DOI: 10.1021/acs.jpcc.8b04385
J. Phys. Chem. C 2018, 122, 15198−15207

decrease, reaching a new plateau. This feature originates from the fact that a localized H motion (such as reorientational motion) leads to only partial averaging of the dipole−dipole interactions.[36] In principle, the high-T plateau value of Δ_H should depend on the mechanism of reorientations. However, for such complex anions as $B_{10}H_{10}^{2-}$, estimates based on the second moment calculations can be considered only as rough guides for a selection of the reorientational models. As in the case of the ordered phase of $Na_2B_{10}H_{10}$,[4] the only physically reasonable reorientational models for ordered monoclinic $Rb_2B_{10}H_{10}$ are related to 90° reorientations around the anion C_4 symmetry axis and 180° flips (of the C_4 axis) concomitant with additional 45° twists (see Figure 5).

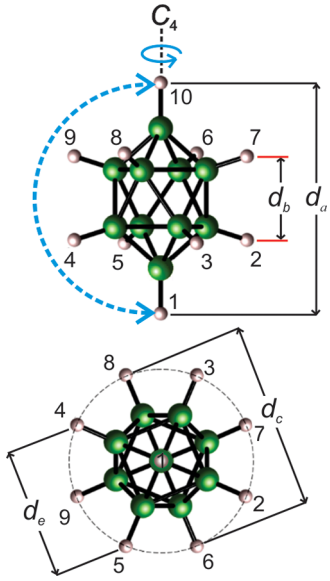

Figure 5. Two views of the bicapped square antiprismatic $B_{10}H_{10}^{2-}$ anions. Green and white spheres denote the respective B and H atoms. H atoms are numbered for convenience. Distances used in this study to represent the "ideal" anion polyhedral size and shape are estimated by averaging the room-temperature NPD results for ordered $Na_2{}^{11}B_{10}D_{10}$ and $^7Li_2{}^{11}B_{10}D_{10}$ from refs 14 and 1. The apical−apical distance (d_a) between H1 and H10 is 6.10 Å. The intraequatorial band, nearest-neighbor H−H atom distance (d_e) between, e.g., H4 and H5 is 3.43 Å. The perpendicular distance, d_b, between the two planes (denoted by light red lines) containing the two equatorial bands of H atoms is 2.31 Å. The band diameter $d_c = \sqrt{2}\,d_e$ = 4.85 Å. The nearest-neighbor interband H−H atom distance (d_j; not shown) between, e.g., H2 and H7 is 2.96 Å. The next-nearest-neighbor interband H atom distance (d_k; also not shown) between, e.g., H2 and H8 is 5.04 Å. The blue arrows indicate the possible anion reorientations in an ordered structure.

Using the expressions derived by Dereppe,[37] we have found that the rotation of the $B_{10}H_{10}^{2-}$ anion around the C_4 axis should lead to a 72% decrease in the "intramolecular" H−B contribution to the second moment with respect to its "rigid-lattice" value. Assuming that the line shape is Gaussian, this corresponds to a 53% drop of the line width. The observed drop of Δ_H for $Rb_2B_{10}H_{10}$ in Figure 4 is considerably stronger; this suggests a presence of an additional type of reorientation. The estimated combined effect of the rotations around the C_4 axis and the 180° flips corresponds to an 88% decrease in the "intramolecular" H−B contribution to the second moment with respect to its "rigid-lattice" value. Such a drop of the second moment corresponds to a 65% drop of Δ_H, which is close to the observed (~75%) drop of Δ_H. These estimates show that the behavior of the ^{1}H NMR line width in $Rb_2B_{10}H_{10}$ is consistent with a complex mechanism of anion reorientations likely involving both rotations around the C_4 symmetry axis and 180° flips as expected. To gain an even more detailed understanding about the nature of the anion reorientational mechanisms, we performed a series of complementary QENS measurements on $Rb_2{}^{11}B_{10}H_{10}$.

Quasielastic Neutron Scattering. Figure 6 shows the neutron elastic-scattering FWS[38] for $Rb_2{}^{11}B_{10}H_{10}$ measured on

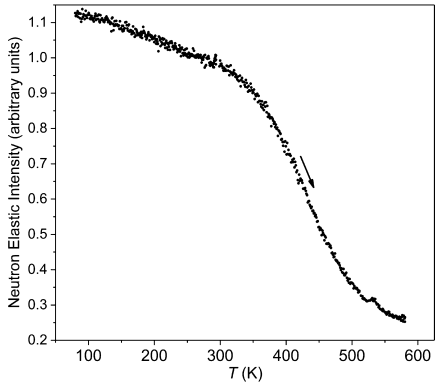

Figure 6. Neutron elastic-scattering FWS (upon heating at 0.5 K min^{-1}) for $Rb_2{}^{11}B_{10}H_{10}$ at Q = 0.87 Å^{-1} measured with 0.8 μeV fwhm instrumental resolution on HFBS.

HFBS at Q = 0.87 Å^{-1} between 80 and 580 K. Upon heating, the accelerated fall-off in intensity beyond normal attenuation from the Debye−Waller factor begins by about 300 K and signals that anion reorientational jump rates are coming into the HFBS resolution window and beginning to exceed 10^7 s^{-1} (and reaching 10^8 s^{-1} by around 350 K), consistent with the NMR results. By the maximum temperature attained of 580 K (limited by the 600.6 K melting point of the Pb sample cell o-ring seal), the fall-off in intensity begins to slow again, signaling that anion reorientational jump rates are now of the order of 10^{10} s^{-1} and moving out of the HFBS dynamic range window. This large range in anion mobilities was subsequently mapped out by complementary measurements on the DCS, HFBS, and NSE instruments.

Figure 7 displays two exemplary QENS spectra for $Rb_2{}^{11}B_{10}H_{10}$ measured at widely different resolutions (at 525 K, Q = 0.6 Å^{-1}, 89 μeV resolution, DCS; and at 510 K, Q = 0.68 Å^{-1}, 0.8 μeV resolution, HFBS). In addition to an elastic peak component, the combination of DCS and HFBS spectra indicates the presence of two quasielastic broadenings on order of magnitude different width scales: a much broader quasielastic component approximated by a single Lorentzian (L_a) [actually comprised of two single mechanism-related Lorentzians (L_{a1} + L_{a2})] in the low-resolution DCS spectrum in Figure 7a and a much narrower single Lorentzian (L_b) clearly evident in the high-resolution HFBS spectrum (above an extremely broad L_a baseline component) in Figure 7b.

An additional exemplary QENS measurement in Figure 8 (at intermediate resolution) is able to distinguish the presence of all different Lorentzian components (L_{a1}, L_{a2}, and L_b) in a single spectrum. In addition to these quasielastic features, the presence of a much broader (>5 meV fwhm Lorentzian equivalent) ubiquitous background component, which be-

DOI: 10.1021/acs.jpcc.8b04385
J. Phys. Chem. C 2018, 122, 15198−15207

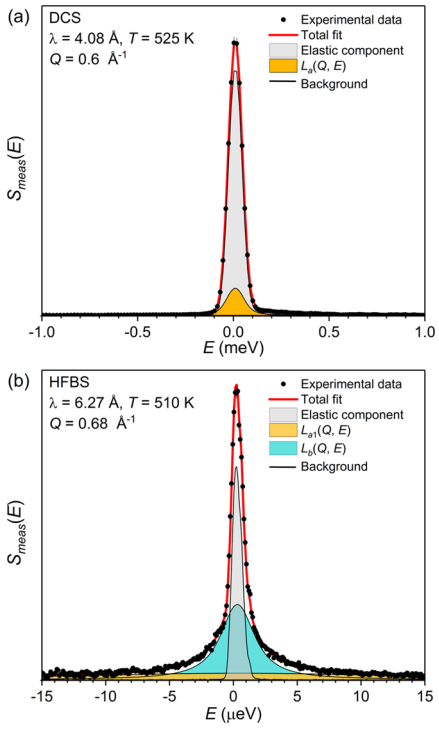

Figure 7. QENS spectra for $Rb_2{}^{11}B_{10}H_{10}$ at (a) 525 K, $Q = 0.6$ Å^{-1}, 89 μeV resolution, on DCS, showing the presence of a broad quasielastic component L_a and (b) 510 K, $Q = 0.68$ Å^{-1}, 0.8 μeV resolution, on HFBS, showing an additional, much narrower, quasielastic component L_b.

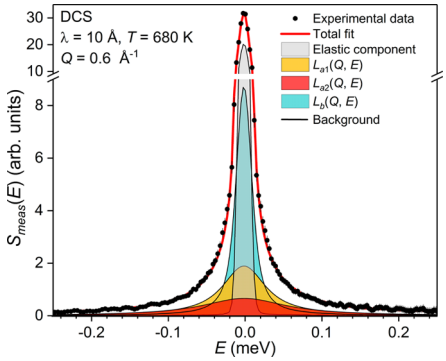

Figure 8. QENS spectrum for $Rb_2{}^{11}B_{10}H_{10}$ at 680 K and $Q = 0.6$ Å^{-1} measured with DCS (10 Å wavelength neutrons; 17 μeV fwhm resolution) delineating the presence of the different Lorentzian components observed in Figure 7a ($L_a \approx L_{a1} + L_{a2}$) and 7b ($L_b$), now all evident in a single spectrum.

comes much more noticeable and intense at higher Q values, (see Figure S5) is reasonably assumed to represent inelastic scattering from overdamped localized oscillatory motions of the anions,[39] a phenomenon routinely observed for other comparable compounds.[4,12] The fit of the overdamped component intensity versus Q data at 580 K in Figure S6 estimates an oscillatory displacement distance of 0.52(3) Å, again in agreement with other comparable compounds.[4,12]

As mentioned in the previous section, there are only two physically reasonable reorientational models (see Figure 5) consistent with one crystallographically unique $B_{10}H_{10}{}^{2-}$ anion in a fully ordered structure such as shown in Figure 1. The first model (designated as C_4) is a single type of reorientational motion involving 90° (fourfold) jumps around the anion C_4 symmetry axis that connects the two apical H atoms. In this case, the H atoms in each of two bands of four equatorial H atoms visit all four positions in their individual band, whereas the two apical H atoms remain immobile, contributing solely to the elastic peak intensity. The second model (designated as C_4 + flip) is an extension of the first model. Here, besides 90° (fourfold) jumps around the anion C_4 symmetry axis, a second reorientational motion is possible, involving 180° rotational flips of the anion so as to exchange positions of the two apical H atoms. Because of the particular D_{4d} molecular symmetry of the anion and the ordered nature of the monoclinic structure, a concomitant 45° "twist" around the C_4 symmetry axis is also required to map the original anion image exactly onto itself. Hence, the trajectory required to attain this reorientational flip may not follow a straightforward rotational motion but rather a more complicated lowest energy barrier pathway. The combination of these two different reorientational motions enables each of the eight equatorial H atoms of the anion to visit all of the other equatorial H crystallographic positions in both bands, whereas the two apical H atoms are restricted to only exchanging apical positions. We focus on these two models during analyses of the QENS data.

The two different QENS components indicated to us that we were indeed observing the two possible types of $B_{10}H_{10}{}^{2-}$ reorientational motions within our neutron resolution window, i.e., C_4 reorientations and flips, with roughly order of magnitude different mobilities. We note that instances of such reorientational behavior involving markedly different mobilities around different anion axes are not uncommon, e.g., highly anisotropic $BH_4{}^-$ anion reorientational mobilities are clearly evident in hexagonal solid solutions of $LiBH_4$ + LiI by both NMR and QENS.[40,41] Based on the ellipsoidal shape of the $B_{10}H_{10}{}^{2-}$ anion, it seemed more likely that the broader Lorentzian component (L_a) reflected more rapid 90° fourfold jumps around the C_4 axis, whereas the narrower component (L_b) reflected much slower 180° orthogonal flips.

Our initial model-independent fits of the broader Lorentzian component from the DCS data indicated an increasing linewidth with increasing Q, roughly doubling by $Q = 2.5$ Å^{-1} with respect to its lowest value, which prevailed below $Q = 0.6$ Å^{-1}. This behavior is consistent with a fourfold jump mechanism, which requires two Lorentzian components L_{a1} and L_{a2} whose fwhm linewidths differ by a factor of two ($\Gamma_{a2} = 2\Gamma_{a1}$) and whose intensities are Q-dependent.[42] The ratio of the L_{a1} and L_{a2} integrated intensities I_{a1} and I_{a2} for such a mechanism is expected to be

$$I_{a1}/I_{a2} = 2[1 - j_0(Q\sqrt{2}\,d_e)]/[1 - 2j_0(Qd_e) + j_0(Q\sqrt{2}\,d_e)] \quad (1)$$

where $j_0(x) = \sin(x)/x$, the zeroth-order spherical Bessel function, and $d_e \approx 3.43$ Å, the nearest-neighbor H−H atom distance within each equatorial band (see Figure 5).

Analyzing the 4.08 Å wavelength DCS data at various temperatures, we successfully fit the broader Lorentzian component as the summation of two Lorentzians, L_{a1} and L_{a2}, with a fixed ratio of fwhm linewidths $\Gamma_{a2} = 2\Gamma_{a1}$ and relative intensities dictated by eq 1 over the entire Q-range measured. At this relatively poor resolution, the much narrower L_b component is largely hidden within the envelope of elastic peak intensity and the reorientational jumps associated with this particular component are effectively frozen

DOI: 10.1021/acs.jpcc.8b04385
J. Phys. Chem. C 2018, 122, 15198−15207

within this neutron resolution window. Hence, we are left to consider what we assume are only the more rapid fourfold C_4 jumps, with relatively immobile apical H atoms.

To better illustrate our mechanistic interpretations of the QENS data, we evaluated the Q-dependent behavior of the elastic incoherent structure factor (EISF), which is defined as the ratio of elastic to elastic + quasielastic scattering intensities. The Q-dependence of the EISF is sensitive to the fundamental details of the reorientational mechanism. The EISFs corresponding to the two possible reorientation models, C_4 and C_4 + flip, were derived elsewhere[4] and are listed below. N.B., all pertinent distances are depicted in Figure 5. For fourfold jumps around the anion C_4 symmetry axis, the EISF is

$$\mathrm{EISF}_{C_4} = \frac{1}{5}[2 + 2j_0(Qd_e) + j_0(Q\sqrt{2}\,d_e)] \tag{2}$$

For fourfold jumps around the C_4 axis + 180° flips orthogonal to the C_4 axis (with a concomitant 45° C_4 twist), the EISF is defined as

$$\mathrm{EISF}_{C_4+\mathrm{flip}} = \frac{1}{10}[2 + j_0(Qd_a) + 2j_0(Qd_e) + j_0(Q\sqrt{2}\,d_e) + 2j_0(Qd_j) + 2j_0(Qd_k)] \tag{3}$$

where $d_a \approx 6.10$ Å, the interapical H−H distance, and d_j and d_k are two different interequatorial band H−H distances with

$$d_j = \left[2\left(d_e \sin\left[\frac{\pi}{8}\right]\right)^2 + {d_b}^2\right]^{1/2} \approx 2.96\ \text{Å} \tag{4}$$

and

$$d_k = \left[2\left(d_e \sin\left[\frac{3\pi}{8}\right]\right)^2 + {d_b}^2\right]^{1/2} \approx 5.04\ \text{Å} \tag{5}$$

In these equations, $d_b \approx 2.31$ Å, the perpendicular distance between the two equatorial bands defined by the two quartets of equatorial H atoms.

The observed EISF behavior is seen to be potentially consistent with both models depending on the particular instrumental resolution employed. For example, again under lower-resolution conditions at 580 K using DCS (4.08 Å neutrons, 89 μeV fwhm resolution), the narrower Lorentzian component L_b is largely buried under the elastic peak. The resulting EISF (with the "invisible" narrower Lorentzian hidden within the envelope of elastic scattering intensity) should therefore only be reflective of the fourfold jumps around the C_4 axis, leading to an EISF more consistent with the C_4 reorientation model. Indeed, Figure 9 shows good agreement between the Q-dependence of the experimentally derived EISF values from the 4.08 Å wavelength DCS data at 580 K and that of the EISF curve for C_4 reorientations generated from eq 2.

This situation changes when the EISF is generated by analyzing the higher-resolution 10 Å DCS data at 600 K with the inclusion of the additional narrow Lorentzian component L_b, assumed to be reflecting slower orthogonal flips. These slower flips are now sensed within the neutron resolution window leading to decreased EISF values in Figure 9 as some fraction of the elastic scattering intensity originally observed using 4.08 Å DCS data is now distinguishable as L_b quasielastic scattering intensity, as exemplified earlier in Figure 8. The resulting EISF is now more consistent with the C_4 + flip model

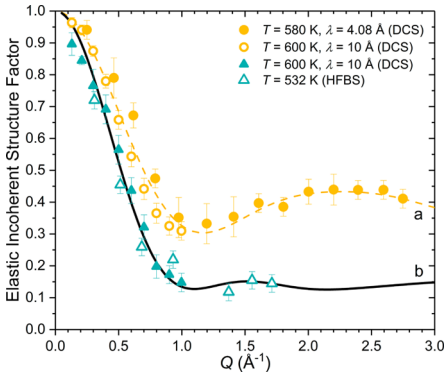

Figure 9. EISF data vs Q for $Rb_2{}^{11}B_{10}H_{10}$ at various temperatures and instrumental conditions. The circles represent EISF values determined assuming only quasielastic scattering from L_a contributions; the triangles represent those determined assuming quasielastic scattering from both L_a and L_b contributions. EISF model curves for the only two reasonable anion reorientational mechanisms are: (a) fourfold jumps around the anion C_4 symmetry axis and (b) fourfold jumps around the C_4 axis + 180° flips orthogonal to the C_4 axis (which also requires a concomitant 45° "twist" around the C_4 symmetry axis to maintain crystallographic order).

curve generated from eq 3. Figure 9 also shows that the calculated EISF values for the 10 Å DCS data revert back to the C_4 model if the L_b quasielastic component is artificially included as part of the total elastic scattering intensity. Finally, the EISF values in Figure 9 determined from the high-resolution HFBS data at 532 K, while including both broad and narrow quasielastic scattering components, further corroborate the C_4 + flip model out to a larger Q value of 1.7 Å^{-1} (well past the 10 Å DCS maximum Q limit), where the model values are expected to plateau.

We further employed much higher-resolution NSE measurements at 380 and 365 K to extend the lower-temperature range accessible to dynamical evaluation and expand the overlap region between the QENS and NMR measurements. As expected, the NSE data at both of these temperatures suggested the presence of more than one jump frequency. For consistency with the DCS and HFBS data analyses, the NSE data were fit (see Figure S6 and accompanying fitting parameters) assuming two broader linewidth-correlated components associated with the proposed C_4 mechanism plus a third independent lower-frequency component due to the 180° flips.

Figure 10 shows plots, in an Arrhenius fashion, of the temperature dependences of the fundamental jump correlation frequencies $[{\tau_{i1}}^{-1} = \Gamma_{i1}/(2\hbar)$, where i denotes a or b components and $\hbar$ is the reduced Planck's constant] for the two different reorientational motions as determined from the three different QENS instruments. Moreover, Figure 10 includes data points from Figure 3 as determined from the NMR measurements.

Some interesting observations can be made about the jump frequency data. First, the jump frequencies for both types of reorientations differ by roughly an order of magnitude between 400 and 680 K and follow linear Arrhenius dependences. The activation energies for reorientation, E_a, were derived from the slopes $(-E_a/k_B)$ of the linear fits to the $\ln({\tau_{i1}}^{-1})$ versus T^{-1} QENS data for $T \geq 400$ K: 197(2) meV for the presumed faster 90° fourfold reorientations and 288(3) meV for the slower 180° flips. Below 400 K, the data from both QENS and

DOI: 10.1021/acs.jpcc.8b04385
J. Phys. Chem. C 2018, 122, 15198−15207

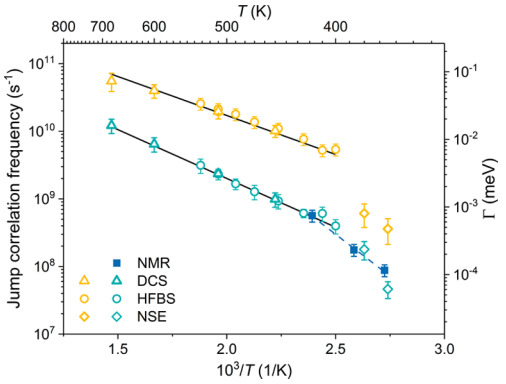

Figure 10. Anion jump correlation frequencies τ_{i1}^{-1} vs inverse temperature for the two different assumed reorientational motions [i = a (90° C_4 reorientations; orange symbols) and b (180° flips; blue symbols)] detected for monoclinic $Rb_2{}^{11}B_{10}H_{10}$. Values for τ^{-1} determined from the complementary NMR data are also included for comparison. Different symbols denote the different instruments used. The solid lines represent linear fits to the QENS data for $T \geq$ 400 K. The dashed line is the linear fit to the NMR data between 367 and 418 K.

NMR suggest that the slopes steepen (i.e., activation energies increase), although there is no evidence of a phase transition in this region. We speculate that the higher apparent barrier in this region stems from enhanced steric effects due to the ever-decreasing unit cell size of the monoclinic structure with decreasing temperature.

From Figure 10, it would appear that the NMR data are chiefly tuned into the slower dynamic (180° anion flips) between 367 and 418 K, whereas the QENS data can distinguish both dynamics. The QENS data for 180° flips nicely overlap the NMR data in this region, largely confirming the steeper 485 meV barrier determined by NMR at these lower temperatures. As the temperature further decreases, one would expect that NMR would eventually tune into the faster C_4 dynamic, but there is no obvious indication from the ^{1}H NMR line narrowing that this is occurring before the jump frequency slows down to roughly 10^5 jumps s^{-1} by 235 K, as estimated from Figure 4. This seems unusual but is not inconsistent with the NSE QENS results for the derived C_4 jump frequencies at 380 and 365 K, which already have dropped much more than expected from an extrapolation of the higher-temperature linear fit of the DCS + HFBS data in Figure 10. The FWS results in Figure 6 also suggest an upper bound for the faster reorientational dynamic of only $\approx 10^8$ jumps s^{-1} at around 350 K (the rough low-temperature limit for HFBS dynamical sensitivity), which is consistent with the NSE results and an order of magnitude smaller than expected from extrapolation to this temperature of the higher-temperature linear fit in Figure 10. Hence, it is probable that the jump frequencies for the two types of reorientational motions are becoming more similar as the temperature approaches 235 K, making it difficult for NMR to distinguish a separate C_4 dynamic in this region.

The activation energy associated with the anion fourfold jumps around the C_4 axis in $Rb_2B_{10}H_{10}$ can be compared with similar compounds. Although there are no reported activation energies for other ordered $M_2B_{10}H_{10}$ congeners (M = Li, Na, K, Cs), there are for the related Li-1-CB_9H_{10} and Na-1-CB_9H_{10} compounds,[4] which possess bicapped square antiprismatic 1-$CB_9H_{10}^-$ anions, identical in shape to $B_{10}H_{10}^{2-}$ anions. The main difference between 1-$CB_9H_{10}^-$ and $B_{10}H_{10}^{2-}$ anions is the substitution of C for B for the former at one of the apical positions. This changes the molecular symmetry from D_{4d} to C_{4v} and the charge from −2 to −1. In an ordered crystallographic phase, each 1-$CB_9H_{10}^-$ anion possesses one energetically preferred orientation within the ordered lattice due to the polarizing nature of the C substituent with respect to the surrounding cations. As such, its symmetry precludes it from performing 180° orthogonal flips of the C_4 axis and it can only undergo fourfold reorientations around its C_4 axis. We previously reported activation energies of 302 and 234 meV, respectively, for ordered Li-1-CB_9H_{10} and Na-1-CB_9H_{10} compounds from analyses of NMR data,[4] which are larger than the 197 meV for $Rb_2B_{10}H_{10}$ and follow the expected trend of decreasing barriers as the size of the cation and unit cell volume increase. This is not a perfect comparison because there are twice as many cations per anion for $M_2B_{10}H_{10}$ than for M-1-CB_9H_{10} compounds, but it is reasonable to assume that more numerous cation neighbors for the former compounds would effectively provide more resistance to reorientation and translate into higher barriers than for the latter compounds when comparing compounds with the same cations. Comparative QENS/NMR studies of an ordered Rb-1-CB_9H_{10} phase would be desirable to address this issue directly.

It would also be interesting to extend comparative QENS studies to include ordered $Rb_2B_{12}H_{12}$, which contains the $B_{12}H_{12}^{2-}$ icosahedral *closo*-polyborate cousin of the $B_{10}H_{10}^{2-}$ anion. A previous QENS study of isomorphic ordered $Cs_2B_{12}H_{12}$ suggests that the $B_{12}H_{12}^{2-}$ anions at lower temperatures actually favor uniaxial reorientations, either 120° threefold jumps around one of the anion C_3 symmetry axes or 72° fivefold jumps around one of the anion C_5 symmetry axes.[43] This is analogous to the more frequent 90° fourfold jumps observed here around the $B_{10}H_{10}^{2-}$ C_4 symmetry axis. As mentioned earlier, NMR has indicated much slower anion reorientational jump dynamics in $Rb_2B_{12}H_{12}$ with respective τ^{-1} values of $\approx 1 \times 10^8$ and $\approx 3 \times 10^9$ s^{-1} at 425 and 550 K.[25] For $Rb_2B_{10}H_{10}$, the comparative 90° fourfold jump frequencies are considerably higher, $\approx 7 \times 10^9$ and $\approx 3 \times 10^{10}$ s^{-1} at these same respective temperatures. Moreover, the $Rb_2B_{12}H_{12}$ activation energy was determined to be 549(5) meV,[25] which is almost double the 288(3) meV value associated with 90° C_4 jumps in $Rb_2B_{10}H_{10}$. Assuming that the NMR data for $Rb_2B_{12}H_{12}$ were indeed reflecting similar uniaxial reorientations as observed by QENS for $Cs_2B_{12}H_{12}$ and $Rb_2B_{10}H_{10}$, then these relative mobilities and barriers make some sense. A larger reorientational barrier and lower-frequency reorientations might reasonably be expected for the more spheroidal-shaped, larger-diameter $B_{12}H_{12}^{2-}$ anions compared to the ellipsoidal-shaped, smaller-diameter $B_{10}H_{10}^{2-}$ anions based on the relative moments of inertia and steric arguments. In short, for a more enlightening comparison, additional QENS measurements would be needed to confirm the nature of the anion reorientations in $Rb_2B_{12}H_{12}$.

CONCLUSIONS

The dynamical behavior of the $B_{10}H_{10}^{2-}$ anion in the ordered monoclinic phase of $Rb_2B_{10}H_{10}$ was characterized by QENS and NMR over a broad temperature range of stability from subambient temperatures to 680 K, confirming the two types of expected reorientational motions that are possible due to the D_{4d} molecular symmetry of the anion, i.e., faster fourfold 90°

DOI: 10.1021/acs.jpcc.8b04385
J. Phys. Chem. C 2018, 122, 15198−15207

reorientational jumps around the anion C_4 symmetry axis and order of magnitude slower 180° orthogonal flips of this axis. It is noteworthy that this reorientational behavior is somewhat similar to that previously observed for the much more highly mobile anions in superionic, disordered $M_2B_{10}H_{10}$ and MCB_9H_{10} (M = Li, Na) compounds.[4] Despite no obvious crystallographic restrictions (based on powder diffraction) on the allowable anion orientations in these disordered compound phases, QENS measurements nonetheless indicated that the individual anions still seemed to favor predominantly uniaxial reorientations around the C_4 symmetry axis at lower temperatures. Yet these reorientations were not necessarily restricted to 90° jumps as for ordered $Rb_2B_{10}H_{10}$ but were rather free to undergo a variety of smaller-angle jumps more akin to uniaxial rotational diffusion. At the higher temperatures, the EISF transformed to reflect a mechanism more consistent with the additional emergence of the familiar 180° flips of the C_4 axis. Yet unlike for ordered $Rb_2B_{10}H_{10}$, it was not possible to isolate distinct disparate quasielastic components marking the relative reorientational jump rates associated with the C_4 uniaxial reorientations and the 180° flips in these disordered compound phases.

■ ASSOCIATED CONTENT

Supporting Information

The Supporting Information is available free of charge on the ACS Publications website at DOI: 10.1021/acs.jpcc.8b04385.

CIF structural file for $Rb_2{}^{11}B_{10}H_{10}$ at 100 K (CIF)
CIF structural file for $Rb_2{}^{11}B_{10}H_{10}$ at 298 K (CIF)
CIF structural file for $Rb_2{}^{11}B_{10}H_{10}$ at 450 K (CIF)
Complementary TGA–DSC, SXRPD, NPD, NVS, and QENS data (PDF)

■ AUTHOR INFORMATION

Corresponding Authors

*E-mail: mirjana.dimitrievska@nist.gov (M.D.).
*E-mail: skripov@imp.uran.ru (Alexander V. Skripov).
*E-mail: udovic@nist.gov (T.J.U.).

ORCID

Mirjana Dimitrievska: 0000-0002-9439-1019
Vitalie Stavila: 0000-0003-0981-0432
Roman V. Skoryunov: 0000-0001-6158-9056
Hui Wu: 0000-0003-0296-5204
Alexander V. Skripov: 0000-0002-0610-5538
Terrence J. Udovic: 0000-0002-9453-2483

Notes

The authors declare no competing financial interest.

■ ACKNOWLEDGMENTS

M.D. and J.D.T. gratefully acknowledge support from the US DOE Office of Energy Efficiency and Renewable Energy, Fuel Cell Technologies Office, under contract no. DE-AC36-08GO28308. This work was performed within the assignment of the Russian Federal Agency of Scientific Organizations (program "Spin" no. AAAA-A18-118020290129-5). Sandia National Laboratories is a multimission laboratory managed and operated by National Technology and Engineering Solutions of Sandia, LLC., a wholly owned subsidiary of Honeywell International, Inc., for the U.S. Department of Energy's National Nuclear Security Administration under contract no. DE-NA-0003525. This work utilized facilities supported in part by the National Science Foundation under agreement nos. DMR-0944772 and DMR-1508249. Use of the Advanced Photon Source, an Office of Science User Facility operated for the US DOE Office of Science by Argonne National Laboratory, was supported by the US DOE under contract no. DE-AC02-06CH11357. The authors thank N. Verdal for performing a portion of the QENS and TGA–DSC experiments.

■ REFERENCES

(1) Tang, W. S.; Dimitrievska, M.; Chotard, J.-N.; Zhou, W.; Janot, R.; Skripov, A. V.; Udovic, T. J. Structural and Dynamical Trends in Alkali-Metal Silanides Characterized by Neutron-Scattering Methods. *J. Phys. Chem. C* **2016**, *120*, 21218–21227.

(2) Remhof, A.; Łodziana, Z.; Buchter, F.; Martelli, P.; Pendolino, F.; Friedrichs, O.; Züttel, A.; Embs, J. P. Rotational Diffusion in $NaBH_4$. *J. Phys. Chem. C* **2009**, *113*, 16834–16837.

(3) Blanchard, D.; Maronsson, J. B.; Riktor, M. D.; Kheres, J.; Sveinbjörnsson, D.; Gil Bardají, E.; Léon, A.; Juranyi, F.; Wuttke, J.; Lefmann, K.; Hauback, B. C.; Fichtner, M.; Vegge, T. Hindered Rotational Energy Barriers of BH4- Tetrahedra in β-$Mg(BH_4)_2$ from Quasielastic Neutron Scattering and DFT Calculations. *J. Phys. Chem. C* **2012**, *116*, 2013–2023.

(4) Soloninin, A. V.; Dimitrievska, M.; Skoryunov, R. V.; Babanova, O. A.; Skripov, A. V.; Tang, W. S.; Stavila, V.; Orimo, S.; Udovic, T. J. Comparison of Anion Reorientational Dynamics in MCB_9H_{10} and $M_2B_{10}H_{10}$ (M = Li, Na) via Nuclear Magnetic Resonance and Quasielastic Neutron Scattering Studies. *J. Phys. Chem. C* **2017**, *121*, 1000–1012.

(5) Verdal, N.; Udovic, T. J.; Stavila, V.; Tang, W. S.; Rush, J. J.; Skripov, A. V. Anion Reorientations in the Superionic Conducting Phase of Na2B12H12. *J. Phys. Chem. C* **2014**, *118*, 17483–17489.

(6) Verdal, N.; Udovic, T. J.; Rush, J. J.; Stavila, V.; Wu, H.; Zhou, W.; Jenkins, T. Low-Temperature Tunneling and Rotational Dynamics of the Ammonium Cations in $(NH_4)_2B_{12}H_{12}$. *J. Chem. Phys.* **2011**, *135*, 094501.

(7) Skripov, A. V.; Skoryunov, R. V.; Soloninin, A. V.; Babanova, O. A.; Stavila, V.; Udovic, T. J. Nuclear Magnetic Resonance Study of Anion and Cation Reorientational Dynamics in $(NH_4)_2B_{12}H_{12}$. *J. Phys. Chem. C* **2018**, *122*, 3256–3262.

(8) Udovic, T. J.; Matsuo, M.; Unemoto, A.; Verdal, N.; Stavila, V.; Skripov, A. V.; Rush, J. J.; Takamura, H.; Orimo, S. Sodium Superionic Conduction in $Na_2B_{12}H_{12}$. *Chem. Commun.* **2014**, *50*, 3750–3752.

(9) Udovic, T. J.; Matsuo, M.; Tang, W. S.; Wu, H.; Stavila, V.; Soloninin, A. V.; Skoryunov, R. V.; Babanova, O. A.; Skripov, A. V.; Rush, J. J.; et al. Exceptional Superionic Conductivity in Disordered Sodium Decahydro-*closo*-decaborate. *Adv. Mater.* **2014**, *26*, 7622–7626.

(10) Lu, Z.; Ciucci, F. Structural Origin of the Superionic Na Conduction in $Na_2B_{10}H_{10}$ *Closo*-Borates and Enhanced Conductivity by Na Deficiency for High Performance Solid Electrolytes. *J. Mater. Chem. A* **2016**, *4*, 17740–17748.

(11) Varley, J. B.; Kweon, K.; Mehta, P.; Shea, P.; Heo, T. W.; Udovic, T. J.; Stavila, V.; Wood, B. C. Understanding Ionic Conductivity Trends in Polyborane Solid Electrolytes from Ab Initio Molecular Dynamics. *ACS Energy Lett.* **2017**, *2*, 250–255.

(12) Dimitrievska, M.; Shea, P.; Kweon, K. E.; Bercx, M.; Varley, J. B.; Tang, W. S.; Skripov, A. V.; Stavila, V.; Udovic, T. J.; Wood, B. C. Carbon Incorporation and Anion Dynamics as Synergistic Drivers for Ultrafast Diffusion in Superionic $LiCB_{11}H_{12}$ and $NaCB_{11}H_{12}$. *Adv. Energy Mater.* **2018**, *8*, 1703422.

(13) Bonnetot, B.; Mongeot, H.; Aboukhassib, A.; Lefebvre, F. Phase Transition Investigations of Closo-Hydroborates. *Inorg. Chim. Acta* **1992**, *193*, 21–26.

(14) Wu, H.; Tang, W. S.; Zhou, W.; Stavila, V.; Rush, J. J.; Udovic, T. J. The Structure of Monoclinic $Na_2B_{10}H_{10}$: a Combined

DOI: 10.1021/acs.jpcc.8b04385
J. Phys. Chem. C 2018, 122, 15198–15207

Diffraction, Spectroscopy, and Theoretical Approach. *CrystEngComm* **2015**, *17*, 3533−3540.
(15) The mention of all commercial suppliers in this paper is for clarity and does not imply the recommendation or endorsement of these suppliers by NIST.
(16) Hofmann, K.; Albert, B. Crystal Structures of $M_2[B_{10}H_{10}]$ (M = Na, K, Rb) via Real-Space Simulated Annealing Powder Techniques. *Z. Kristallogr.* **2005**, *220*, 142−146.
(17) Toby, B. H.; Von Dreele, R. B. GSAS-II: The Genesis of a Modern Open-Source All Purpose Crystallography Software Package. *J. Appl. Crystallogr.* **2013**, *46*, 544−549.
(18) Larson, A. C.; Von Dreele, R. B. *General Structure Analysis System, Report LAUR 86−748*; Los Alamos National Laboratory: NM, 1994.
(19) Stalick, J. K.; Prince, E.; Santoro, A.; Schroder, I. G.; Rush, J. J. Materials Science Applications of the New National Institute of Standards and Technology Powder Diffractometer. In *Neutron Scattering in Materials Science II*; Neumann, D. A., Russell, T. P., Wuensch, B. J., Eds.; Materials Research Society: Pittsburgh, 1995; Vol. *376*, pp 101−106.
(20) Udovic, T. J.; Brown, C. M.; Leão, J. B.; Brand, P. C.; Jiggetts, R. D.; Zeitoun, R.; Pierce, T. A.; Peral, I.; Copley, J. R. D.; Huang, Q.; Neumann, D. A.; Fields, R. J. The Design of a Bismuth-Based Auxiliary Filter for the Removal of Spurious Background Scattering Associated with Filter-Analyzer Neutron Spectrometers. *Nucl. Instrum. Methods Phys. Res., Sect. A* **2008**, *588*, 406−413.
(21) Copley, J. R. D.; Cook, J. C. The Disk Chopper Spectrometer at NIST: A New Instrument for Quasielastic Neutron Scattering Studies. *Chem. Phys.* **2003**, *292*, 477−485.
(22) Meyer, A.; Dimeo, R. M.; Gehring, P. M.; Neumann, D. A. The High-Flux Backscattering Spectrometer at the NIST Center for Neutron Research. *Rev. Sci. Instrum.* **2003**, *74*, 2759−2777.
(23) Rosov, N.; Rathgeber, S.; Monkenbusch, M. Neutron Spin Echo Spectroscopy at the NIST Center for Neutron Research. In *Scattering from Polymers: Characterization by X-rays, Neutrons, and Light*; Cebe, P., Hsaio, B. S., Lohse, D. J., Eds.; American Chemical Society Symposium Series; American Chemical Society, 1999; Vol. *739*, pp 103−116.
(24) Azuah, R. T.; Kneller, L. R.; Qiu, Y.; Tregenna-Piggott, P. L. W.; Brown, C. M.; Copley, J. R. D.; Dimeo, R. M. DAVE: A Comprehensive Software Suite for the Reduction, Visualization, and Analysis of Low Energy Neutron Spectroscopic Data. *J. Res. Natl. Inst. Stand. Technol.* **2009**, *114*, 341−358.
(25) Skripov, A. V.; Babanova, O. A.; Soloninin, A. V.; Stavila, V.; Verdal, N.; Udovic, T. J.; Rush, J. J. Nuclear Magnetic Resonance Study of Atomic Motion in $A_2B_{12}H_{12}$ (A = Na, K, Rb, Cs): Anion Reorientations and Na+ Mobility. *J. Phys. Chem. C* **2013**, *117*, 25961−25968.
(26) Giannozzi, P.; Baroni, S.; Bonini, N.; Calandra, M.; Car, R.; Cavazzoni, C.; Ceresoli, D.; Chiarotti, G. L.; Cococcioni, M.; Dabo, I.; Dal Corso, A.; de Gironcoli, S.; Fabris, S.; Fratesi, G.; Gebauer, R.; Gerstmann, U.; Gougoussis, C.; Kokalj, A.; Lazzeri, M.; Martin-Samos, L.; Marzari, N.; Mauri, F.; Mazzarello, R.; Paolini, S.; Pasquarello, A.; Paulatto, L.; Sbraccia, C.; Scandolo, S.; Sclauzero, G.; Seitsonen, A. P.; Smogunov, A.; Umari, P.; Wentzcovitch, R. M. QUANTUM ESPRESSO: A Modular and Open-Source Software Project for Quantum Simulations of Materials. *J. Phys.: Condens. Matter* **2009**, *21*, 395502.
(27) Kresse, G.; Furthmüller, J.; Hafner, J. Ab initioForce Constant Approach to Phonon Dispersion Relations of Diamond and Graphite. *Europhys. Lett.* **1995**, *32*, 729−734.
(28) Yildirim, T. Structure and Dynamics from Combined Neutron Scattering and First-Principles Studies. *Chem. Phys.* **2000**, *261*, 205−216.
(29) Momma, K.; Izumi, F. VESTA 3 for Three-Dimensional Visualization of Crystal, Volumetric and Morphology Data. *J. Appl. Crystallogr.* **2011**, *44*, 1272−1276.
(30) Verdal, N.; Wu, H.; Udovic, T. J.; Stavila, V.; Zhou, W.; Rush, J. J. Evidence of a Transition to Reorientational Disorder in the Cubic Alkali-Metal Dodecahydro-*Closo*-Dodecaborates. *J. Solid State Chem.* **2011**, *184*, 3110−3116.
(31) Skripov, A. V.; Skoryunov, R. V.; Soloninin, A. V.; Babanova, O. A.; Tang, W. S.; Stavila, V.; Udovic, T. J. Anion Reorientations and Cation Diffusion in $LiCB_{11}H_{12}$ and $NaCB_{11}H_{12}$: ^1H, ^7Li, and ^{23}Na NMR Studies. *J. Phys. Chem. C* **2015**, *119*, 26912−26918.
(32) Abragam, A. *The Principles of Nuclear Magnetism*; Clarendon Press: Oxford, 1961.
(33) Markert, J. T.; Cotts, E. J.; Cotts, R. M. Hydrogen Diffusion in the Metallic Glass a-$Zr_3RhH_{3.5}$. *Phys. Rev. B: Condens. Matter Mater. Phys.* **1988**, *37*, 6446−6452.
(34) Skripov, A. V.; Soloninin, A. V.; Babanova, O. A.; Hagemann, H.; Filinchuk, Y. Nuclear Magnetic Resonance Study of Reorientational Motion in α-Mg(BH4)2. *J. Phys. Chem. C* **2010**, *114*, 12370−12374.
(35) Skripov, A. V. Hydrogen Diffusion in Laves-Phase Compounds. *Defect Diffus. Forum* **2003**, *224−225*, 75−92.
(36) Skripov, A. V.; Soloninin, A. V.; Babanova, O. A.; Skoryunov, R. V. Nuclear Magnetic Resonance Studies of Atomic Motion in Borohydride-Based Materials: Fast Anion Reorientations and Cation Diffusion. *J. Alloys Compd.* **2015**, *645*, S428−S433.
(37) Dereppe, J. M. Second Moment Expressions for Solids Containing Reorienting Nuclear Spins. *J. Chem. Phys.* **1973**, *58*, 1254−1255.
(38) Udovic, T. J.; Verdal, N.; Rush, J. J.; De Vries, D. J.; Hartman, M. R.; Vajo, J. J.; Gross, A. F.; Skripov, A. V. Mapping Trends in the Reorientational Mobilities of Tetrahydroborate Anions via Neutron-Scattering Fixed-Window Scans. *J. Alloys Compd.* **2013**, *580*, S47−S50.
(39) Dieterich, W.; Peschel, J.; Schneider, W. R. Diffusion in Periodic Potentials. *Z. Phys. B: Condens. Matter Quanta* **1977**, *27*, 177−187.
(40) Skripov, A. V.; Soloninin, A. V.; Rude, L. H.; Jensen, T. R.; Filinchuk, Y. Nuclear Magnetic Resonance Studies of Reorientational Motion and Li Diffusion in $LiBH_4$-LiI Solid Solutions. *J. Phys. Chem. C* **2012**, *116*, 26177−26184.
(41) Verdal, N.; Udovic, T. J.; Rush, J. J.; Wu, H.; Skripov, A. V. Evolution of the Reorientational Motions of the Tetrahydroborate Anions in Hexagonal $LiBH_4$-LiI Solid Solution by High-Q Quasielastic Neutron Scattering. *J. Phys. Chem. C* **2013**, *117*, 12010−12018.
(42) Bée, M. *Quasielastic Neutron Scattering, Principles and Applications in Solid State Chemistry, Biology and Materials Science*; Adam Hilger: Bristol, 1988.
(43) Verdal, N.; Udovic, T. J.; Rush, J. J.; Cappelletti, R. L.; Zhou, W. Reorientational Dynamics of the Dodecahydro-closo-dodecaborate Anion in $Cs_2B_{12}H_{12}$. *J. Phys. Chem. A* **2011**, *115*, 2933−2938.

DOI: 10.1021/acs.jpcc.8b04385
J. Phys. Chem. C 2018, 122, 15198−15207